

Monitoring Polar Sea Ice Using Optical and SAR Data

AUTHORS

Hequan Sun

Dalian Naval Academy,
Dalian, China

Chunhua Li

Key Laboratory of Research on
Marine Hazards Forecasting,
National Marine Environmental
Forecasting Center, Beijing, China

Yifeng Cheng

Dalian Naval Academy,
Dalian, China

ABSTRACT

With the movement and destructiveness of sea ice, conventional *in situ* instruments are restricted or unavailable for polar sea ice observation. Satellite remote sensing is a feasible way to monitor sea ice in the polar area. Multispectral imaging spectrometer and synthetic aperture radar are applied to monitoring the sea ice in this article with high spatial resolution, wide swath, and continuous imaging. The sea ice distribution and motion can be measured by analyzing satellite remote sensing images. The image segmentation method is presented in the article to obtain the sea ice distribution. Meanwhile, the cross-correlation algorithm to extract sea ice motion is proposed as well as the processed vector results.

Keywords: remote sensing, sea ice concentration, sea ice motion, image segmentation, cross-correlation

Introduction

Polar sea ice forms an interface between the upper part of the ocean and the lower part of the atmosphere. Sea ice changes the radiation balance and energy balance on the ocean surface and isolates the heat exchange and water vapor exchange between the ocean and the atmosphere. The freezing and thawing process of sea ice affects the formation and intensity of ocean currents. Polar sea ice plays an important role in the global climate system.

Meanwhile, sea ice is a major barrier for ship traffic in the polar area. Sea ice floes are dangerous for most ships and fishing vessels. It is also difficult for icebreakers and ice-strengthened vessels to navigate the area with high sea ice concentration and thick ice. One typical case is that Chinese icebreaking research vessel *Snow Dragon*, which was trapped in thick ice floes during an international Antarctic rescue mission in January 2014. With the opening of the polar ship-

ping routes and polar resource utilization, more attention is paid to navigation safety in the polar area, and polar ice monitoring is one of the important factors.

Because of the low temperature, strong winds, and the movement and potential destructive nature of sea ice floes, conventional *in situ* oceanographic measuring techniques are restricted or unavailable in the polar area. Under these circumstances satellite remote sensing is the only feasible method to monitor the ocean parameters with high spatial resolution. Polar ice parameters such as ice concentration, ice thickness, ice surface temperature, ice emissivity, snow on ice, sea ice drift, and so on, can be observed or estimated by remote sensing sensors such as multispectral imaging spectrometers, microwave radiometers, microwave scatterometers, radar altimeters, synthetic aperture radar (SAR), and so forth. Meanwhile, the polar area can be mapped in overlap mode by the sun-synchronous

polar orbiting satellite, and data with higher sampling frequency and fine grid can be obtained than that in low latitudes.

The sea ice distribution and its concentration can be calculated by applying image segmentation methods to satellite images. The sea ice motion can be estimated by analyzing the satellite remote sensing images with motion estimation methods (Flores et al., 1995; Liu & Zhao, 1999; Thomas et al., 2008, 2011; Hollands & Dierking, 2011; Sun et al., 2015).

In this article, the image segmentation method and motion estimation method are presented in detail, and some optical and SAR satellite remote sensing images are provided to validate the performance of the proposed methods.

Basics

Sea Ice Segmentation Algorithm

Since there is a significant difference in color, intensity, and reflectivity

between sea ice and sea water/land, sea ice can be discriminated in satellite images by using image segmentation methods, and sea ice distribution and concentration can be calculated.

Optimal thresholding segmentation is an effective tool to separate the object from the background in image processing. The effect of image segmentation depends on the choice of threshold value. The Otsu method based on discriminant analysis is one of the most popular classical segmentation algorithms, which maximizes the gray level histogram variance to obtain the best separation of classes (Otsu, 1979; Xu et al., 2011).

Let the satellite image histogram be represented in L levels: $[g_{\min}, g_{\min} + \delta_g, \Lambda, g_{\max}]$, where g_{\min} is the gray level minimum, g_{\max} is the gray level maximum, and $\delta_g = \frac{g_{\max} - g_{\min}}{L - 1}$. The probability of occurrence at the i th level is $p_i = \frac{n_i}{N} \geq 0$ and $\sum_{i=1}^L p_i = 1$, where n_i is the number of gray level values located in $[g_{\min} + (i - 1) \cdot \delta_g, g_{\min} + i \cdot \delta_g]$ and N is the total number of image pixels.

Suppose that the satellite image pixels can be dichotomized into two classes, C_0 and C_1 (background and sea ice), by a threshold up to k th level, C_0 and C_1 denotes the satellite image pixels with levels $[g_{\min}, g_{\min} + \delta_g, \Lambda, g_{\min} + (k - 1) \cdot \delta_g]$ and $[g_{\min} + k \cdot \delta_g, \Lambda, g_{\max}]$, respectively. The probability of occurrence and the histogram mean of class C_0 are $\omega(k) = \Pr(C_0) = \sum_{i=1}^k p_i$ and $\mu(k) = \sum_{i=1}^k (i \cdot p_i)$, and the total histogram mean is $\mu_T = \sum_{i=1}^L (i \cdot p_i)$, respectively.

The optimal level k^* meets the relationship of $\sigma_B^2(k^*) = \max_{1 \leq k < L} \frac{[\mu_T \cdot \omega(k) - \mu(k)]^2}{\omega(k) \cdot [1 - \omega(k)]}$, and the threshold value to dichotomize the background and sea ice is given as $g_t = g_{\min} + (k^* - 1) \cdot \delta_g$.

Sea ice segmentation from the satellite image involves two steps. In the first step, median filtering is applied to the image for reducing pepper noise. Second, the Otsu segmentation method is applied in calculating the threshold value, and the satellite image is separated into two parts by comparing the pixel value with the threshold .

Sea Ice Motion Estimation Method

The sea ice velocity field can be estimated from the displacements of the sea floes in two images between two instances of time. Since an individual floe cannot be detected easily and accurately in the remote sensing images, the subarea matching is adopted in this article. The sea ice motion estimation methods include cross-correlation methods (Thomas et al., 2008; Hollands & Dierking, 2011; Sun et al. 2015) and optical flow methods (Gutierrez & Long, 2003; Bruhn et al., 2005; Sun et al., 2016). According to the authors' experience, cross-correlation methods are preferred because the sea ice floes can be treated as rigid objects. Meanwhile, optical flow methods are quite time consuming.

The subarea of the first remote sensing image at t_1 can be assumed as $p(x, y) = f(x, y)$ to represent the pixel intensity, and that of the second remote sensing image at t_2 can be expressed as $q(x, y) = f(x - \Delta x, y - \Delta y)$ with the displacement of $(\Delta x, \Delta y)$. The cross-correlation function of $p(x, y)$ and $q(x, y)$, and the autocorrelation function of $f(x, y)$ are defined as

$$\begin{cases} r_{pq}(\tau_x, \tau_y) = \int_{-\infty}^{+\infty} \int_{-\infty}^{+\infty} p(x, y) \cdot q(x + \tau_x, y + \tau_y) dx dy \\ r_{ff}(\tau_x, \tau_y) = \int_{-\infty}^{+\infty} \int_{-\infty}^{+\infty} f(x, y) \cdot f(x + \tau_x, y + \tau_y) dx dy \end{cases} \quad (1)$$

Then,

$$r_{pq}(\tau_x, \tau_y) = r_{ff}(\tau_x - \Delta x, \tau_y - \Delta y) \quad (2)$$

Because any autocorrelation function is even and the maximum value is located at the original point, the inequality can be derived as $r_{pq}(\tau_x, \tau_y) \leq r_{pq}(\Delta x, \Delta y)$. The displacement during $\Delta t = t_2 - t_1$ can be estimated to be $(\Delta x, \Delta y)$ from the maximum position of the cross-correlation function. Scaling this displacement with the geographical factor, the sea ice motion can be calculated quantitatively. The cross-correlation can be implemented efficiently by the fast Fourier transform or the fast Hartley transform (Sun, 2002) as demonstrated below.

Fast Algorithm of Cross-Correlation

With the kernel function $\text{cas}(\omega t) = \cos(\omega t) + \sin(\omega t)$, the two-dimensional Hartley transform and its inverse transform with the odd and even parts are defined as

$$\begin{cases} P(u, v) = \int_{-\infty}^{+\infty} \int_{-\infty}^{+\infty} p(x, y) \text{cas}(ux) \text{cas}(vy) dx dy \\ p(x, y) = \int_{-\infty}^{+\infty} \int_{-\infty}^{+\infty} P(u, v) \text{cas}(ux) \text{cas}(vy) du dv \end{cases}. \quad (3)$$

$$\begin{cases} P_o(u, v) = \frac{1}{2}[P(u, v) - P(-u, -v)] \\ P_e(u, v) = \frac{1}{2}[P(u, v) + P(-u, -v)] \end{cases}. \quad (4)$$

The cross-correlation operation in the temporal domain is equivalent to the arithmetic operation in the Hartley domain (Sun, 2002),

$$R_H(u, v) = P_{He}(u, v)Q_{He}(u, v) - P_{Ho}(-u, v)Q_{Ho}(u, -v) + P_{He}(-u, v)Q_{Ho}(u, v) - P_{Ho}(u, v)Q_{He}(u, -v), \quad (5)$$

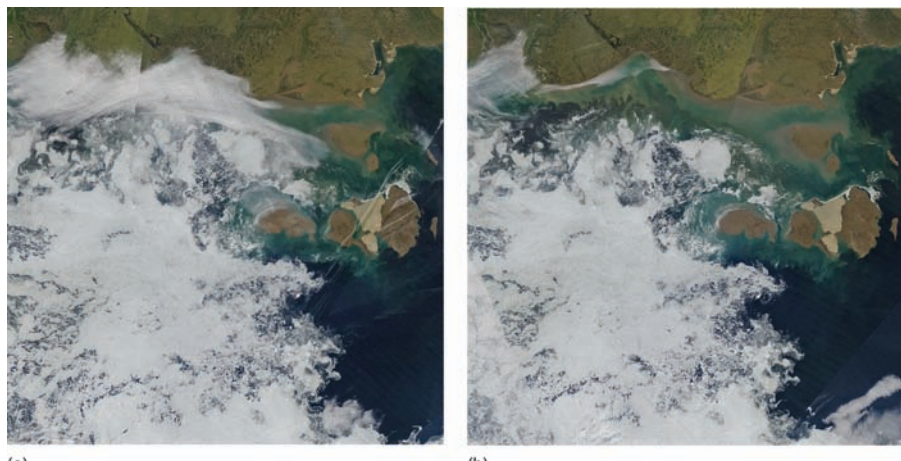
where $R_H(u, v)$, $P_H(u, v)$, and $Q_H(u, v)$ are the Hartley transform of r_{pq} (τ_x , τ_y), $p(x, y)$, and $q(x, y)$ in Eq. (1), respectively, and the suffix o and e indicate the odd and even parts defined in Eq. (4). The cross-correlation can be calculated by two forward transforms and one inverse transform.

Satellite Data and Preprocessing Operation

There are two types of remote sensing images that can be used for high-resolution sea ice analysis—one is the optical and infrared remote sensing image, and the other is SAR image. The optical and infrared images used in the article can be accessed from LANCE-MODIS (Land, Atmosphere

FIGURE 1

Optical images obtained from MODIS/Terra: (a) Arctic_r05c03.2018222.terra.250m and (b) Arctic_r05c03.2018223.terra.250m.



Near Real-Time Capability for EOS–Moderate Resolution Imaging Spectroradiometer) data system operated by the GSFC Terrestrial Information Systems Laboratory (LANCE-MODIS, 2018), and the SAR images can be accessed from Polar View (Karvonen et al., 2007), which is the organization for the provision of operational, satellite-based monitoring of the polar regions and the cryosphere (Polar View, 2018).

Optical Data

LANCE-MODIS can provide near-real-time optical and infrared MODIS data sampled by Aqua and Terra, and true-color or pseudocolor images can be generated by choosing different spectrometer bands. Polar View is an international consortium providing a wide variety of satellite earth observation products in the polar region and parts of midlatitude regions that monitor sea ice cover, glacier runoff, snow cover, snow melt, icebergs, river ice, and lake ice. Accurate and real-time cost-saving information can be found at the Polar View website (<http://polarview.org/>).

True-color MODIS images with the spatial resolution of 250 m, captured on August 10 and 11, 2018 (source: <http://lance-modis.eosdis.nasa.gov>), is shown in Figure 1, and the map coordinate system is WGS 1984 NSIDC Sea Ice Polar Stereographic North.

SAR Data

SAR instruments can work at all weather, day and night, and the optical payloads can only observe the sea surface with good lighting conditions, without cloud contamination. It is clear that the quality of SAR sea ice

FIGURE 2

SAR images obtained from Radarsat2: (a) generated at 20140412 01:35:57 and (b) generated at 20140413 04:24:37.

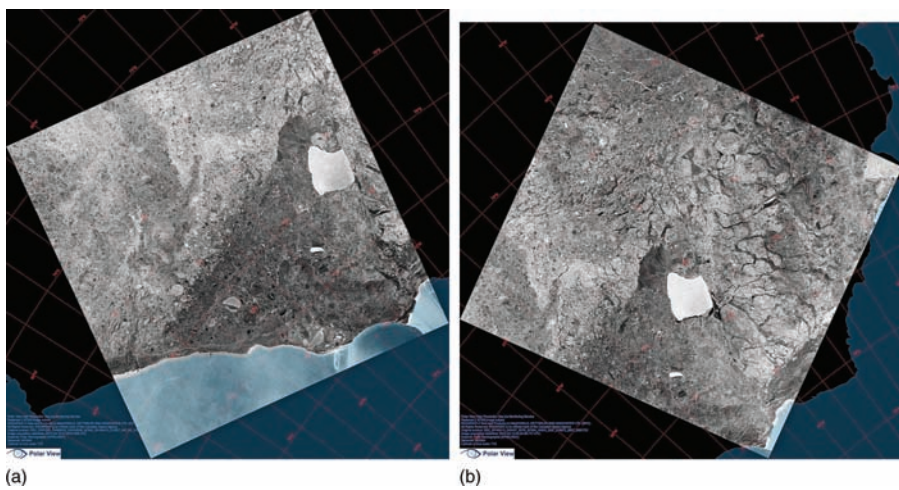


FIGURE 3

Geographical matched SAR images in Figure 2: (a) generated at 20140412 01:35:57 and (b) generated at 20140413 04:24:37.

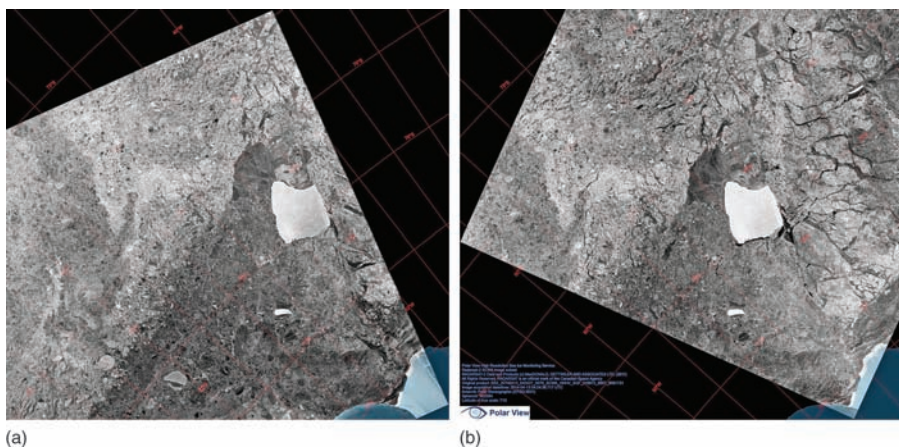
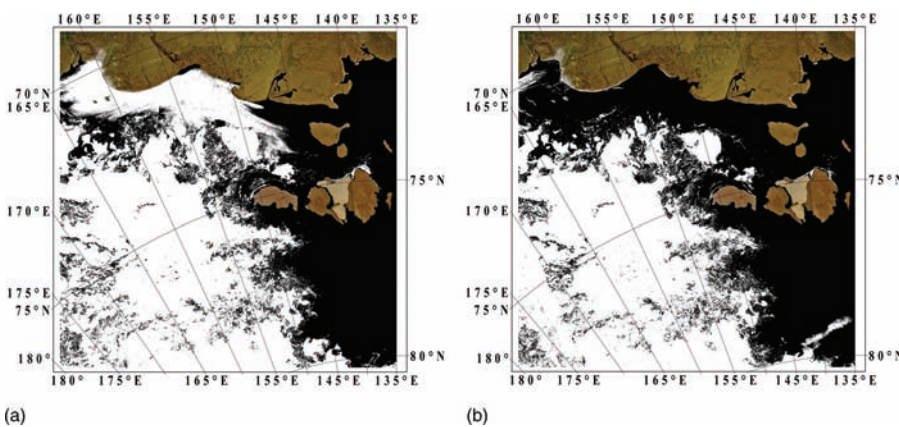


FIGURE 4

MODIS image segmentation performed on image in Figure 1: (a) image segmentation in Figure 1(a) and (b) image segmentation in Figure 1(b).



images is better than that of MODIS images.

High-resolution SAR images can be downloaded from <http://www.polarview.aq>. The images provided by the website have been calibrated, and up-to-the-minute images are provided. The images are categorized according to the region, time sequence, and so on (Polar View, 2018). Two SAR images generated by Radarsat2 are illustrated in Figure 2, where the giant white object is a grounded iceberg named as A23A with a size as large as 44×40 nautical miles. The map coordinate system is WGS 1984 Antarctic Polar Stereographic.

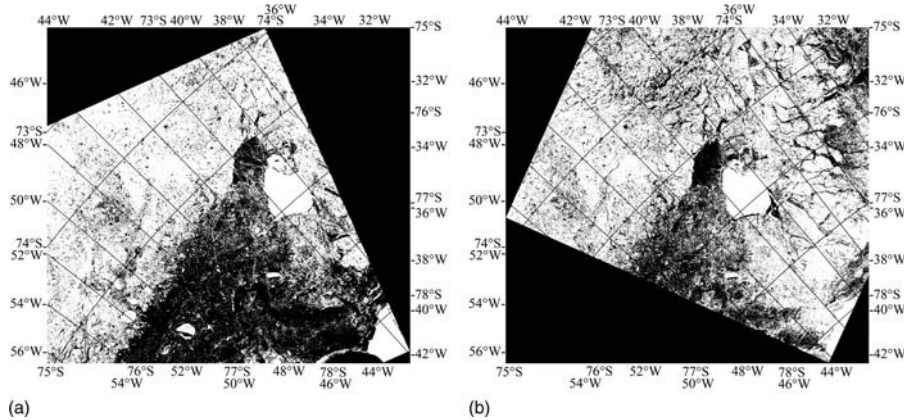
Geographical Matching

There is a little difference between Figures 1 and 2. The geographical matching operation is applied to Figure 2 to get the same region with the same spatial resolution for the next sea ice motion estimation. The images in Figure 2 with the overlapped area can be used to calculate the sea ice motion vectors. The map overlaid with latitude and longitude lines can be extracted from the satellite image, which is orthogonal to each other. Concerned as X-junctions (Chu et al., 2013; Pham et al., 2014; Hansard et al., 2014), the intersections of the map lines in Figure 2 can be detected automatically and accurately for matching and zooming the satellite images. The geographically matched images are illustrated in Figure 3.

During software implementation, a grid of interrogation areas is built with the same size within each satellite image. The size of the interrogation area is set to be greater than twice the estimated sea ice displacement. The corresponding interrogation areas are then processed quickly

FIGURE 5

SAR image segmentation performed on image in Figure 3: (a) image segmentation in Figure 3(a) and (b) image segmentation in Figure 3(b).



with the help of the fast algorithm of cross-correlation, and the mean velocity between two interrogation areas is obtained. This process is repeated at each grid point within the satellite images, resulting in a map of velocity vectors to describe the polar sea ice motion.

Results

Applying the segmentation and cross-correlation methods described

in the previous section to the remote sensing sea ice images, the sea ice distribution and motion can be obtained.

Sea Ice Distribution

The segmentation results of MODIS and SAR images in Figures 1 and 3 are illustrated in Figures 4 and 5 with the latitude and longitude labels. There are some fake regions in Figure 4 because the difference between sea ice

and clouds cannot be distinguished by the Otsu segmentation method. The SAR image segmentation is not affected by clouds or other atmospheric phenomena. According to the segmentation results, the size distribution and concentration of sea ice can be calculated easily for operational application.

Sea Ice Motion

Applying cross-correlation method to MODIS images in Figure 1 and SAR images in Figure 3, the velocity vector maps can be calculated as illustrated in Figures 6 and 7. It is obvious that the mesoscale sea ice dipole vortex and dynamic eddy can be discovered with the detailed information in Figures 6 and 7.

Validation

The long-term drift of sea ice in polar regions has been introduced in many earlier studies (Emery et al., 1997; Holland & Kwok, 2012; Kwok et al., 2013), and the results provided in the article are similar to the

FIGURE 6

Velocity vector map of sea ice motion derived from Figure 1.

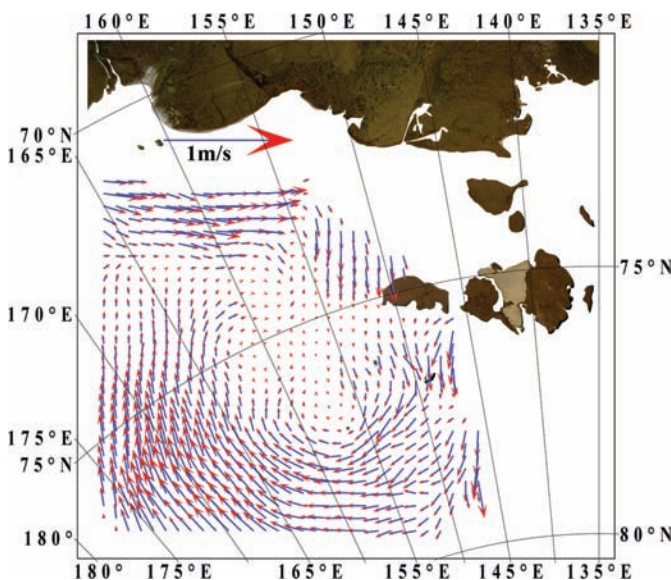
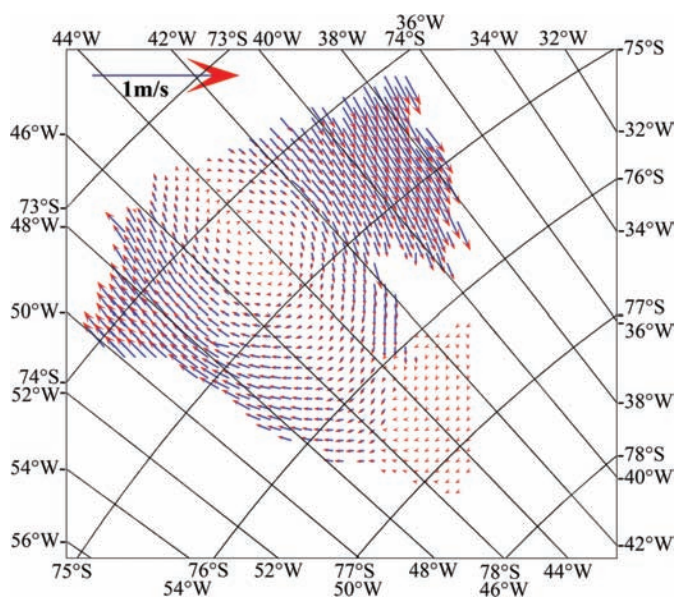


FIGURE 7

Velocity vector map of sea ice motion derived from Figure 1.



results in some previous literature from the trend of thesea ice drift. The validation is conducted with the medium resolution sea ice drift product from 2018-08-10 05:37 to 2018-08-11 05:16 in the Arctic region and the low-resolution sea ice drift product from 2014-04-12 12:00 to 2014-04-14 12:00 in the Antarctic region of the EUMETSAT Ocean and Sea Ice Satellite Application Facility (<http://www.osi-saf.org/>), which the continuous maximum cross-correlation is applied to motion tracking (Lavergne et al., 2010). The sea ice drift products are illustrated in Figures 8 and 9 with the map coordinate system of Oblique Mercator projection.

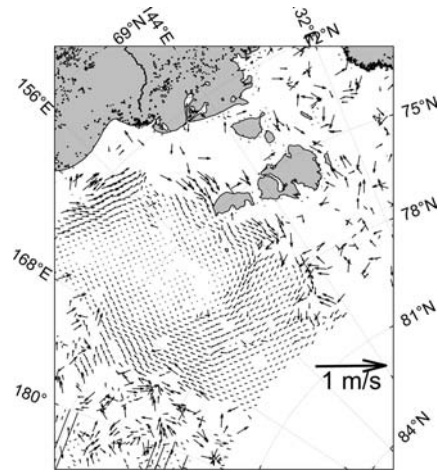
Comparing Figures 6 and 8 with Figures 7 and 9, the distribution of the sea ice drift velocity and direction are basically consistent, which can validate the reliability of the analysis results provided in the article.

Conclusions and Prospects

It is useful for navigation safety to monitor polar sea ice distribution and motion by analyzing satellite remote

FIGURE 8

OSI-SAF sea ice drift product in the Arctic region.



sensing images. The sea ice distribution can be calculated by the image segmentation methods, and the sea ice motion can be derived by calculating the cross-correlation function of the satellite remote sensing images. The mesoscale sea ice dynamic phenomena can be inferred from the velocity vector map clearly with the detailed information, which is helpful for the study of polar sea ice dynamics. Compared with optical remote sensing images, the SAR images are more suitable for polar sea ice monitoring in the region covered by clouds and fog.

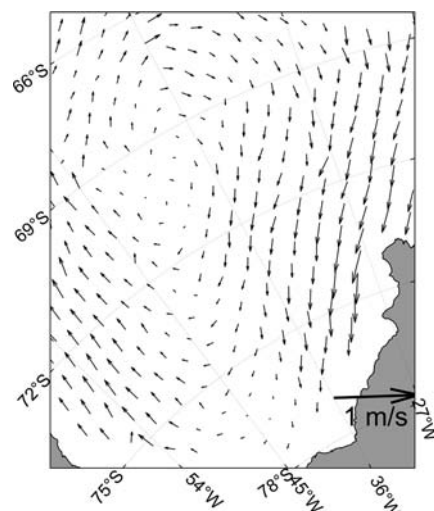
Since the sea ice distribution and motion is caused by the topographic, atmospheric, and oceanic forcing, the results in a given polar area calculated by the proposed methods can be used as initial conditions and applied to the polar sea ice forecasting by combining numerical meteorological and oceanic modeling.

Acknowledgments

We acknowledge the use of data products or imagery from the Land,

FIGURE 9

OSI-SAF sea ice drift product in the Antarctic region.



Atmosphere Near Real-Time Capabilities for EOS (LANCE) system operated by NASA's Earth Science Data and Information System with funding provided by NASA Headquarters. We also acknowledge the use of data products or imagery from Polar View powered by PARABOLA and WORDPRESS.

Corresponding Author:

Hequan Sun
Dalian Naval Academy
No. 667 Jiefang Road,
Zhongshan District
Dalian 116018, China
Email: hqsun@dlut.edu.cn

References

- Bruhn**, A., Weickert, J., & Schnörr, C. 2005. Lucas/Kanade meets Horn/Schunck: combining local and global optic flow methods. *Int J Comput Vision*. 61(3):211-31. <https://doi.org/10.1023/B:VISL.0000045324.43199.43>.
- Chu**, J., Guo, A., & Wang, L. 2013. Chessboard corner detection under image physical coordinate. *Opt Laser Technol*. 48:599-605. <https://doi.org/10.1016/j.optlastec.2012.11.010>.
- Emery**, W.J., Fowler, C.W., & Maslanik, J.A. 1997. Satellite-derived maps of Arctic and Antarctic sea ice motion: 1988 to 1994. *Geophys Res Lett*. 24(8):897-900. <https://doi.org/10.1029/97GL00755>.
- Flores**, M., Maitre, H., & Parmiggiani, F. 1995. Sea-ice velocity fields estimation on Ross Sea with NOAA-AVHRR. *IEEE T Geosci Remote*. 33(5):1286-9. <https://doi.org/10.1109/36.469494>.
- Gutierrez**, S., & Long, D.G. 2003. Optical flow and scale-space theory applied to sea-ice motion estimation in Antarctica. In: *Geoscience and Remote Sensing Symposium* (pp. 2805-7). Toulouse, France: IEEE. <https://doi.org/10.1109/IGARSS.2003.1294592>.
- Hansard**, M., Radu, H., Michel, A., & Evangelidis, G. 2014. Automatic detection

- of calibration grids in time-of-flight images. *Comput Vis Image Und.* 121:108-18. <https://doi.org/10.1016/j.cviu.2014.01.007>.
- Holland**, P.R., & Kwok, R. 2012. Wind-driven trends in Antarctic sea-ice drift. *Nat Geosci.* 5(11):872-5. <https://doi.org/10.1038/ngeo1627>.
- Hollands**, T., & Dierking, W. 2011. Performance of a multiscale correlation algorithm for the estimation of sea-ice drift from SAR images: Initial results. *Ann Glaciol.* 52(57):311-7. <https://doi.org/10.3189/172756411795931462>.
- Karvonen**, J., Haapala, J., Lehtiranta, J., & Seina, A. 2007. Polarview@FIMR: WWW-based delivery of Baltic sea ice products to end-users. In: IEEE International Geoscience and Remote Sensing Symposium (IGARSS). pp. 1242-5. Barcelona, Spain: IEEE. <https://doi.org/10.1109/IGARSS.2007.4423031>.
- Kwok**, R., Spreen, G., & Pang, S. 2013. Arctic sea ice circulation and drift speed: Decadal trends and ocean currents. *J Geophys Res Oceans.* 118:2408-25. <https://doi.org/10.1002/jgrc.20191>.
- LANCE-MODIS**. 2018. Available at: <http://lance-modis.eosdis.nasa.gov/imagery/subsets/?mosaic=Arctic> (accessed December 20, 2018).
- Lavergne**, T., Eastwood, S., Teffah, Z., Schyberg, H., & Breivik, L.-A. 2010. Sea ice motion from low resolution satellite sensors: An alternative method and its validation in the Arctic. *J Geophys Res.* 115:C10032. <https://doi.org/10.1029/2009JC005958>.
- Liu**, A.K., & Zhao, Y. 1999. Arctic sea ice drift from wavelet analysis of NSCAT and special sensor microwave imager data. *J Geophys Res.* 104(C5):11529-38. <https://doi.org/10.1029/1998JC00115>.
- Otsu**, N. 1979. A threshold selection method from gray-level histograms. *IEEE T Syst Man Cyb.* 9(1):62-6. <https://doi.org/10.1109/TSMC.1979.4310076>.
- Pham**, T.A., Delalandre, M., Barrat, S., & Ramel, J. Y. 2014. Accurate junction detection and characterization in line-drawing images. *Pattern Recogn.* 47:282-95. <https://doi.org/10.1016/j.patcog.2013.06.027>.
- Polar View**. 2018. Available at: <http://www.polarview.aq> (accessed December 20, 2018).
- Sun**, H. 2002. The Hartley transform applied to particle image velocimetry. *Meas Sci Technol.* 13:1996-2000. <https://doi.org/10.1088/0957-0233/13/12/326>.
- Sun**, H., Song, Q., Shao, R., & Schlicke, T. 2016. Estimation of sea surface currents based on ocean color remote-sensing image analysis. *Int J Remote Sens.* 37(21):5105-21. <https://doi.org/10.1080/01431161.2016.1226526>.
- Sun**, H., Wang, J., & Zhang, Z. 2015. Sea ice drift monitoring based on SAR imagery. *Sea Technol.* 56(5):45-7.
- Thomas**, M., Geiger, C.A., & Kambhamettu, C. 2008. High resolution (400 m) motion characterization of sea ice using ERS-1 SAR imagery. *Cold Reg Sci Technol.* 52:207-23. <https://doi.org/10.1016/j.coldregions.2007.06.006>.
- Thomas**, M., Kambhamettu, C., & Geiger, C. 2011. Motion tracking of discontinuous sea ice. *IEEE T Geosci Remote.* 49(12):5064-79. <https://doi.org/10.1109/TGRS.2011.2158005>.
- Xu**, X., Xu, S., Jin, L., & Song, E. 2011. Characteristic analysis of Otsu threshold and its applications. *Pattern Recogn Lett.* 32:956-61. <https://doi.org/10.1016/j.patrec.2011.01.021>.